PCCP

ROYAL SOCIETY OF CHEMISTRY

PAPER

View Article Online
View Journal | View Issue

Cite this: *Phys. Chem. Chem. Phys.*, 2025, **27**, 11558

Charge transfer within excited states of boron/nitrogen doped polycyclic aromatic hydrocarbons†

Luan G. F. dos Santos, [a] Julio C. V. Chagas, [cd] Reed Nieman, [a] Adelia J. A. Aquino, [b] Francisco B. C. Machado *[cd] and Hans Lischka *[a]

Polycyclic aromatic hydrocarbons (PAHs) have attracted significant attention in scientific research due to their unique electronic properties and potential applications in various fields such as photovoltaics and photocatalysis. In this study, the excited states and intramolecular charge transfer mechanisms within boron/nitrogen (B/N) doped PAHs using a 5-armchair,5-zig-zag periacene as model were investigated. Starting with a pristine periacene sheet, twelve chemically modified structures were explored, with different topologies of boron and nitrogen doping. Geometry optimization calculations in the ground state were performed at the ωB97XD/def2-SV(P) level, followed by single-point calculations of the low-lying singlet excited states using multireference MR-CISD and SC-NEVPT2 methods and single reference (SR) ADC(2) and TD-DFT theories for comparison. The analysis of energy spectra and charge transfer (CT) character were conducted using the one particle density matrices, analyzing the involved natural transition orbitals (NTOs) and through the decomposition of the states into contributions of local excitations (LE), charge transfer (CT) or double excitations (2-el.) A S_1 CT state was characterized for three of the suggested doped PAHs. Interestingly, in one of these cases, the CT state was dominated by a double excitation character. Beyond this case, it turned out that most of the other excitations also have a strong double excitation component. This fact makes MR calculations highly desirable for accurate investigations, as SR methods such as ADC(2) and TD-DFT become questionable in many cases.

Received 15th February 2025,
Accepted 13th May 2025

DOI: 10.1039/d5cp00618j

rsc.li/pccp

1. Introduction

With the ongoing global warming on earth, energy generation from sustainable energy sources poses huge problems.[1–3] Photocatalytic water splitting to produce hydrogen driven by solar radiation constitutes one major solution for resolving energy bottlenecks.[4] The photocatalytic process is considered to occur in three main steps, divided into (i) light absorption by the catalyst, (ii) generation of hole–electron pairs and (iii) surface oxidation and reduction reactions to produce hydrogen.[5] Photocatalysis, with its capacity to utilize sunlight for driving chemical reactions, presents significant potential for sustainable applications, including pollution remediation and renewable energy production. Consequently, photocatalytic processes offer a viable pathway to cleaner air, water, and energy sources, helping to mitigate the adverse effects of pollution and resource depletion.[6–12]

Polycyclic aromatic hydrocarbons (PAHs) stand at the forefront of contemporary materials research, attracting scientific attention owing to their unique electronic structure and versatile applications across various fields, such as OLEDs, solar-cells and photovoltaics.[13–18] It has been shown that the properties of PAHs can be tuned by chemical doping using heteroatoms, which modify the character of the pi-conjugated system by the introduction of structural defects.[19–24] In photocatalytic applications, defects such as vacancies (holes) and electron states can be created by insertion of electron-rich and electron-deficient heteroatoms into the photocatalyst. Among popular candidates, boron, nitrogen, phosphorus, oxygen, and sulfur play an important role.[25–32] B/N doping in photocatalysis has been discussed in particular[33] and graphene activated with BN

[a] *Department of Chemistry and Biochemistry, Texas Tech University, Lubbock, Texas 79409, USA. E-mail: hans.lischka@ttu.edu*
[b] *Department of Mechanical Engineering, Texas Tech University, Lubbock, Texas 79409, USA*
[c] *Departamento de Química, Instituto Tecnológico de Aeronáutica, 12228-900, São José dos Campos, SP, Brazil. E-mail: fmachado@ita.br*
[d] *Laboratório de Computação Científica Avançada e Modelamento (Lab – CCAM), Instituto Tecnológico da Aeronáutica, 12228-900, José dos Campos, São Paulo, Brazil*

† Electronic supplementary information (ESI) available. See DOI: https://doi.org/10.1039/d5cp00618j

domains have been used successfully for photocatalytic hydrogen generation.[34] Such doped systems are conveniently used because of good light-absorption capabilities and tunability of the band gap.[35–39]

The understanding and control of the creation of hole–electron pairs and their separation forms is one of the most important steps in developing photocatalytically active materials. After creation of an exciton, charge transfer (CT) states will be involved which allow the hole–electron separation at polar boundaries[40] with following chemical oxidation and reduction reactions as indicated above. To create these polar boundaries, B/N doping seems to be promising for that purpose. The goal of this work is to show for different B/N doped PAH model systems the occurrence of low-lying CT states, which have the capability to interact *e.g.* with water molecules (or other reagents) to perform photocatalytic oxidation and reduction processes. In these doping processes, boron acts as an electron acceptor in the π orbital space due to its vacant p_z orbital and graphitic nitrogen performs as electron donor contributing two electrons to the conjugated π system. As basic PAH medium, the (5 armchair (a),5 zig-zag (z)) periacene (Fig. 1(a)) will be used as a paradigmatic class of finite graphene flakes. Similar to acenes,[41–43] periacenes rapidly acquire open shell character[42,44,45] which is located primarily on the zig-zag edges.[42] The armchair edge does not participate in the creation of open shell character. Pristine periacenes themselves provide a good starting point but do not show the prospect for the creation of CT excited states with localized holes and electrons. To induce the creation of the CT states, different B/N doping topologies have been created by insertion of borazine ring chains and B/N lines, respectively. The most interesting cases are shown in Fig. 1(a) displaying the pristine (5a,5z) periacene, and Fig. 1(b) insertions of horizontal and vertical borazine chains, complete borazine edge doping and edge line doping. Nine other structures, to be shown below, have been investigated as well.

The reliable calculation of excited states of PAHs is a difficult task and preferably requires multireference (MR) methods.[46] For that purpose, MR configuration interaction with singles and doubles (MR-CISD) and the strongly-contracted N-electron valence state second order perturbation theory (SC-NEVPT2) calculations have been performed. Additionally, popular single reference methods such as the algebraic diagrammatic construction of second order (ADC(2)) and the time dependent density functional theory (TD-DFT) methods have been performed as well. The purpose of these latter calculations was to explore the potential usage of computationally cheaper methods but also to document eventual shortcomings.

2. Computational details

Geometry optimizations in the ground state were performed at DFT level, with the ωB97XD[47] functional, employing def2-SV(P) basis set.[48] Using these geometries, single point calculations, at MR-CISD level,[49,50] were performed, applying the size extensivity correction of Pople[51] (MR-CISD+P) for the energies and MR-CISD values for oscillator strengths and other wavefunction-derived quantities. Furthermore, single point time dependent density functional theory (TD-DFT), second order algebraic diagrammatic construction (ADC(2))[52,53] and the strongly-contracted n-electron valence state second order perturbation theory (SC-NEVPT2)[54] methods were also computed. The four lowest singlet excited states were computed using all four levels of theory, with the aim of accurately characterizing the lowest bright state and identifying any charge-transfer (CT) states. Resolution of identity approximation[55,56] and the def2-SV(P) basis[48] in combination with the def2-SV(P) auxiliary basis were used for the single-point calculations at TD-DFT, ADC(2) and SC-NEVPT2 levels. The molecular orbitals (MOs) for the SC-NEVPT2 and MR-CISD calculations were obtained from a state-averaged multiconfiguration self-consistent-field (SA-MCSCF) calculation, with a complete active space of 8 orbitals and 8 electrons (CAS(8,8)). This active space was chosen based on

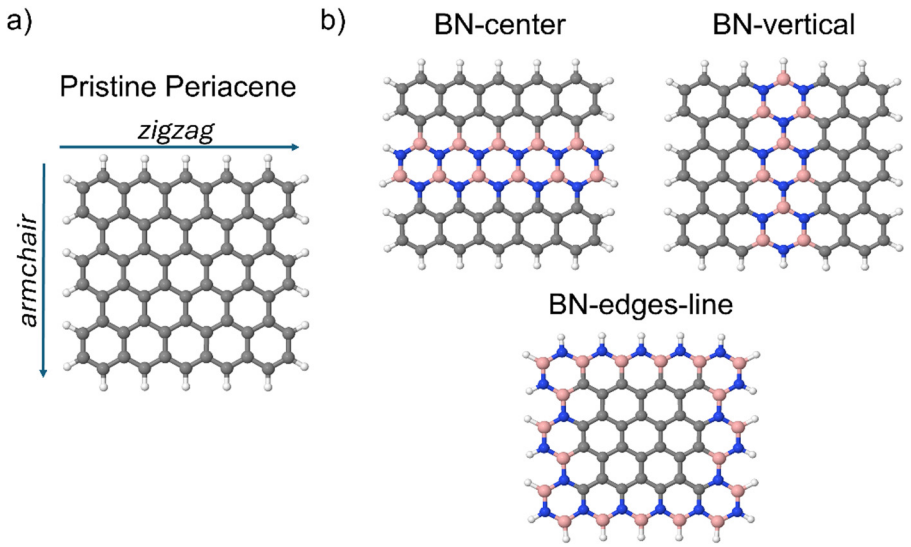

Fig. 1 (a) Framework for the (5a,5z) pristine periacene. (b) Selected B/N doping examples: BN-center, BN-vertical and BN-edges-line.

the previous experience for describing the multiradical character of periacenes.[42] For the D_{2h} structures, the eight π orbitals, corresponding to the b_{3u}, b_{1g}, b_{2g} and a_u irreducible representations were chosen according to natural orbital (NO) occupations. For each of the four irreducible representations, the highest occupied (HONO) and the weakest occupied NO (LUNO) were included. The same pattern of inclusion was adopted for the C_{2v} structures, considering b_1 and a_2 irreducible representations, with two HONOs and two LUNOs each. To reduce the computational effort in the uncontracted MR-CISD calculations, all occupied and virtual σ orbitals were frozen at the MCSCF and MR-CISD levels. It has been shown previously[57] that this approximation worked well for different electronic excitations in the triangular structures phenalenyl and triangulene. The 6-31G[58] basis set was employed for the MR-CISD calculations. The successful applicability of this basis set had been tested before for a series of radical and biradical systems.[57] To further validate the use of the 6-31G basis set in the MR-CISD calculations, additional basis set tests using the polarized 6-31G* basis were performed for a selected set of structures studied in this work. For that purpose, the three structures with low-lying CT states (BN-center, BN-vertical and BN-edges-line) had been chosen. To make these calculations feasible, as a first step, the reference space was compacted guided by the natural orbital occupations found for these structures. Based on the NO occupations, the original CAS(8,8) was partitioned into a CAS(4,4), a restricted active space (RAS) containing the two most strongly occupied orbitals of the original CAS, and an auxiliary space (AUX) including the two weakly occupied ones, resulting in a RAS(2)CAS(4,4)AUX(2) space. Single and double excitations were allowed from RAS to CAS and AUX, and from CAS to AUX orbitals. The excitation energies obtained with this reduced scheme and using the 6-31G basis showed close agreement within a few hundredths of an eV with those from the original CAS(8,8)/6-31G calculations. Based on this validation, MR-CISD calculations using the 6-31G* basis and the reduced reference space were performed. The excitation energies showed very good agreement with the ones obtained with the 6-31G basis, well justifying the use of the smaller 6-31G basis. A comparison of the excitation energies between all three setups is provided in Table S1 of the ESI.†

To describe electronic character of excited states, in particular concerning CT character, hole–electron mappings were used as defined by omega matrices $\Omega_{AB}^{n,\alpha}$ [59,60] according to eqn (1) to characterize the transition from state n to state α by defining molecular fragments of the molecule. In this context, $n = 0$ signifies the transition from the ground state. These mappings are derived from analyzing the one-particle transition density matrix $D^{n\alpha,[AO]}$ from state n to state α in an atomic orbital (AO) basis.

$$\Omega_{AB}^{n,\alpha} = \frac{1}{2}\sum_{\substack{a\in A\\ b\in B}} \left(D^{n\alpha,[AO]}S^{[AO]}\right)_{ab}\left(S^{[AO]}D^{n\alpha,[AO]}\right)_{ab} \quad (1)$$

In eqn (1), A and B denote molecular fragments, $S^{[AO]}$ is the overlap matrix in the atomic orbital (AO) basis and a and b label atomic orbitals. In the present calculations, the electronic excitations start from the ground state, *i.e.* $n = 0$. The total CT[61] for a system with multiple fragments is given by eqn (2)

$$qCT = \frac{1}{\Omega^{n,\alpha}}\sum_{A}\sum_{B\neq A}\Omega_{AB}^{n,\alpha} \quad (2)$$

where

$$\Omega^{n,\alpha} = \sum_{A,B}\Omega_{AB}^{n,\alpha} \quad (3)$$

$qCT = 1$e indicates a complete CT of one electron. While a value equal zero indicates a local excitation of an excitonic state where hole–electron pair is located on the same fragment. Although, instead of calculating the total CT, the individual $\Omega_{AB}^{n,\alpha}$ contributions will be visualized in the form of state composition bar plots. In case of $A = B$ in eqn (1) $\Omega_{AB}^{n,\alpha}$ represents the weight of a local excitation (LE) in A; for $A \neq B$ $\Omega_{AB}^{n,\alpha}$ denotes the weight of an $A \rightarrow B$ charge transfer. The specific segment choices will be explained in the Results section for each doping case separately. The value of $\Omega^{n,\alpha}$ will be taken as a measure for single excitation *vs.* double excitation character.[62] A doubly (or higher) excited state character will lead to a value of $\Omega^{n,\alpha} = 0$ since the one-particle density matrix will vanish whereas a purely singly excited state will have $\Omega^{n,\alpha} = 1$. Intermediate values measure the relative importance of both excitation types. For a detailed discussion on the characterization of double excitations we refer to ref. 62. Furthermore, natural transition orbitals (NTOs)[63] are used for visual representation of the electronic transitions and the natural transition orbital participation ratio (PR_{NTO}) analysis was also conducted. The PR_{NTO} quantity is defined as

$$PR_{NTO} = \frac{\left(\sum_i \lambda_i\right)^2}{\sum_i \lambda_i^2} \quad (4)$$

in which λ_i represents the weight of each transition from the hole to the electron orbital. The PR_{NTO} value indicates how many key NTOs are involved, which reflects the number of configurations necessary to characterize the excited state.

MR-CISD calculations were performed using the COLUMBUS program system,[64,65] SC-NEVPT2 was conducted using ORCA;[66] TD-DFT and ADC(2) calculations were performed using TURBOMOLE.[67] State composition bar plots of excited states, NTO plots and PR_{NTO} values were calculated with the TheoDORE program.[60,68] Oscillator strengths for NEVPT2 calculations were actually calculated at the CASSCF level, which was used as the reference wavefunction for the NEVPT2 calculation.

3. Results and discussion

3.1 The vertical excitation spectrum

The ground-state geometries of all analyzed structures, optimized with ωB97XD/def2-SV(P), are presented in Fig. 2 and the Cartesian Coordinates are provided in the ESI.† Twelve different types of modifications were analyzed, in which the radical properties of eleven of them were previous investigated by our group.[69] They are

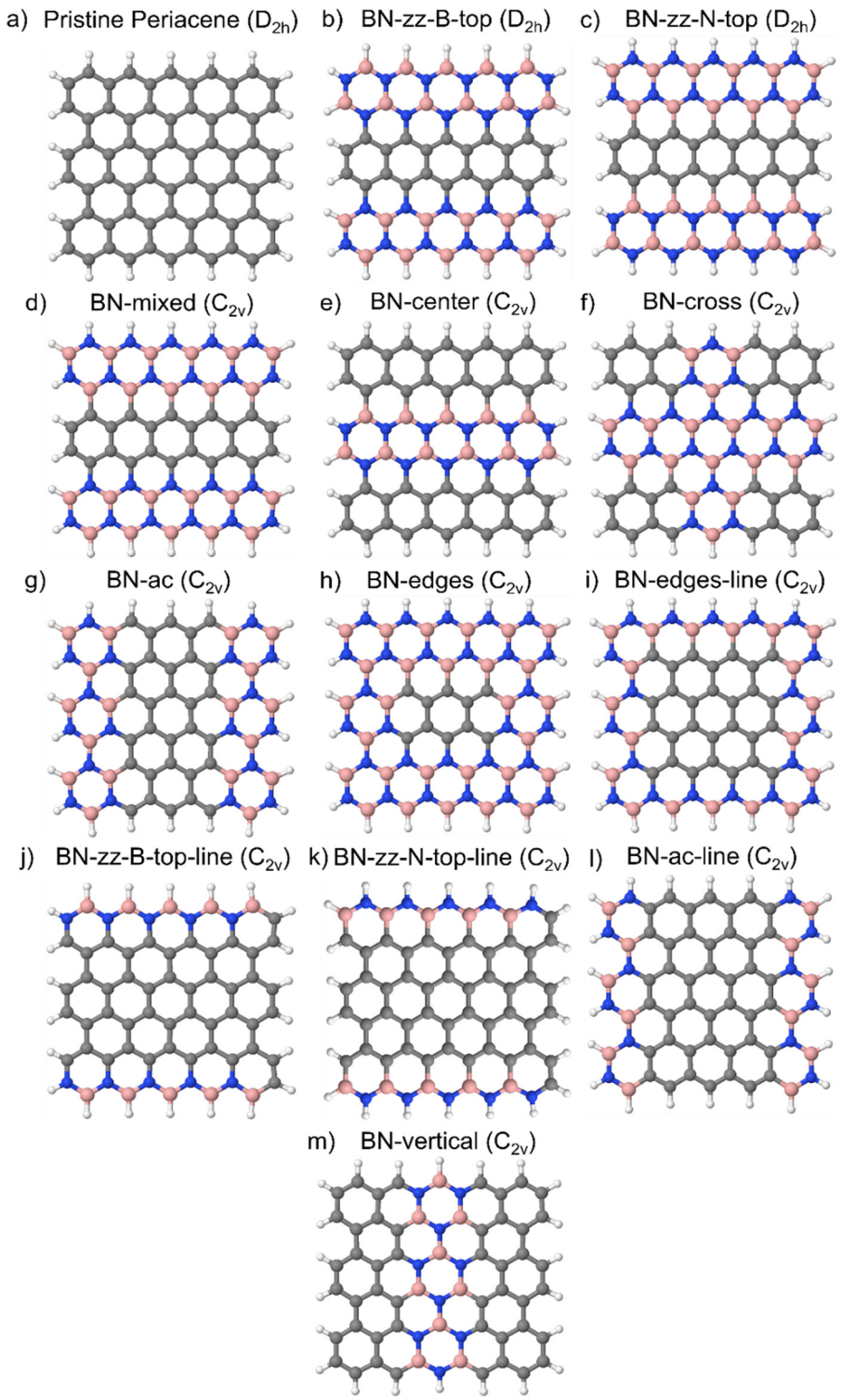

Fig. 2 Structures of the pristine (5a,5z) pristine periacene and the different partially B/N doped periacenes. Respective names are given on top of each structure. Structures a, b and c were optimized in D_{2h} symmetry, whereas all others were in C_{2v}. Atomic color code: grey – carbon, white – hydrogen, blue – nitrogen and pink – boron.

based on the insertion of condensed borazine rings and on the implantation of boron/nitrogen pairs. The proposed insertions, in the form of condensed borazine rings, occur in the rows of the upper and lower edges (BN-zz-B-top, BN-zz-N-top, BN-zz-mixed), the central row (BN-center), in a cross shape (BN-cross), in the armchair lines (BN-ac), at the edge rings of the pristine structure (BN-edges), and in the central vertical row (BN-vertical). Structures based on modification *via* B/N pairs occurred at the edges

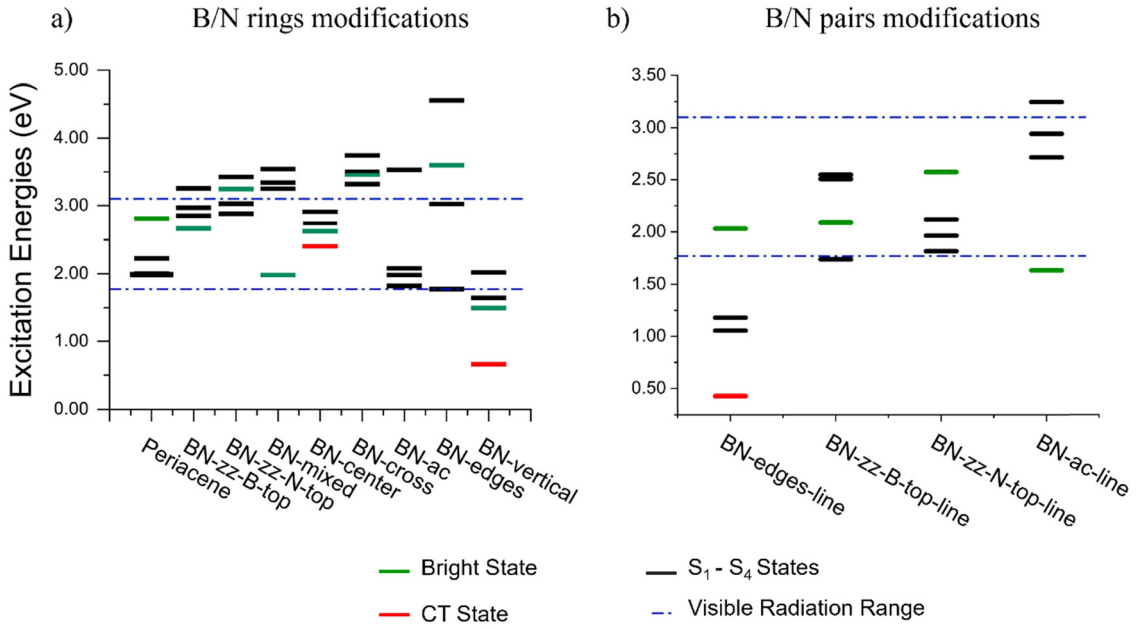

Fig. 3 Excitation energies (eV), obtained at MR-CISD+P level of theory, for the pristine and all doped periacene structures. Green denotes a bright state (highest value of $f > 0.1$), while red specifies a CT state. The dashed lines indicate the visible radiation window.

(BN-edges-line), in the upper and lower rows (BN-zz-B-top-line, BN-zz-N-top-line), and in the armchair row (BN-ac-line). In our previous work,[69] we found varying degrees of open–shell character depending on the doping modification, with S–T splittings below 0.3 eV for BN-ac, BN-edges-line, BN-zz-B-top-line, and BN-zz-N-top-line indicating strong open shell character. Only the BN-vertical structure had not been considered previously. Therefore, its S–T splitting was computed in the present work at the same level of theory (MR-CISD+P/6-31G*) as before. The computed value of 0.33 eV also indicates significant open shell character.

Fig. 3 shows the vertical excitation energies calculated at MR-CISD+P level for the first four singlet excited states of all the studied structures. In Fig. 3(a) the results for the B/N ring modified structures are presented, while Fig. 3(b) analyses this data for the structures modified by line B/N insertions. Numerical data of the excitation energies, PR_{NTO} values and oscillator strengths (f) obtained at MR-CISD+P/MR-CISD level for each individual structure can be found in the ESI† material, in Tables S2–S14. Comparison is made in these tables also with results obtained at NEVPT(2), TD-DFT and ADC(2) levels of theory. Overall, the excitation energies obtained by the latter group of methods follow the same trend shown by MR-CISD+P but are usually somewhat smaller. The bright state for the pristine periacene, as determined by MR-CISD calculations, is S_4 and this level of theory will serve as the reference result for all further analysis. The NEVPT2 calculation also identifies S_4 as the bright state while TD-DFT assigns S_1 as the bright state, deviating from the MR-CISD and NEVPT2 results. For the BN-zz-B-top, BN-zz-N-top and BN-mixed structures, the computed bright states were S_1, S_3 and S_1, respectively, at MR-CISD level. For the three above-mentioned structures, all methods show agreement with the MR-CISD results. Regarding BN-center framework, MR-CISD indicates S_2 as a bright state in agreement with NEVPT2 and ADC(2) calculations. On the other hand, TD-DFT points to the S_1 state. MR-CISD method reveals S_2 as the bright state for the BN-cross structure and both NEVPT2 and TD-DFT agree, while ADC(2) indicates S_3. No bright state was found within the four BN-ac low-lying excited states at MR-CISD level; neither NEVPT2 nor TD-DFT calculations do so as well. For BN-edges and BN-edges-line structures, S_3 and S_4 are bright states at MR-CISD level, and the other methods agree. For the BN-zz-B-top-line structure S_2 is the bright state at MR-CISD level and only ADC(2) indicates the same, while TD-DFT and NEVPT2 indicates S_1 and S_3 states, respectively. In the BN-zz-N-top-line case, MR-CISD result characterizes S_4 as the bright state and from the other methods only NEVPT2 agrees, while ADC(2) and TD-DFT indicates S_2 and S_1, respectively. Analyzing the BN-ac-line structure, S_1 is the bright state at MR-CISD level, and all other methods considered agree. For the BN-vertical case, MR-CISD result states S_3 as the bright state and NEVPT2 agrees; TD-DFT points to the S_1 state. Charge transfer character localized in the S_1 state (indicated by the red traces in Fig. 3) will be further discussed below.

The energetic location of the bright state is of relevance for the utilization of sunlight by the different doped systems. About 40% of the solar radiation received at the earth's surface on clear days is visible radiation (VR) within the spectral range of 1.77 to 3.10 eV[70] (indicated by the horizontal blue dashed line in Fig. 3(a) and (b)). Looking at the excitation energies of all structures, exhibited in Fig. 3, one can see that the periacene, BN-zz-B-top, BN-mixed, BN-center, BN-edges-line, BN-zz-B-top-line and BN-zz-N-top-line structures have a bright state within the visible light radiation range. The bright states for the BN-cross and BN-edge are located in the UV region belonging to the

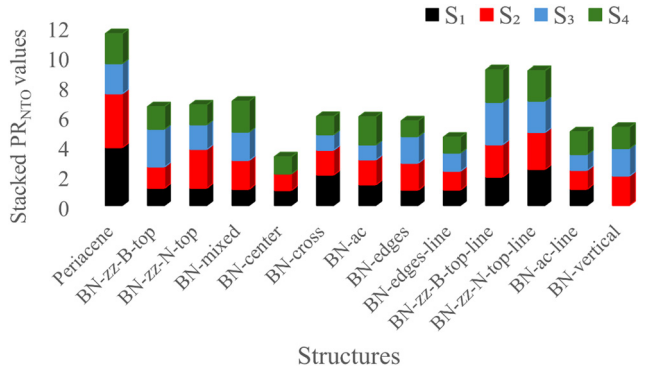

Fig. 4 PR_{NTO} values are shown for all computed excited states and all analyzed structures, obtained at MR-CISD level of theory.

UV-A category (3.10–3.90 eV),[71] which reaches earth once the radiation passes through the ozone layer. Therefore, these states can also be populated by incidence of solar radiation.

The analysis of the MR-CISD wavefunction of excited states offers interesting insight to judge the applicability of other methods, primarily of single-reference character. Here, two descriptors are used for that purpose, PR_{NTO} values and the double-excitation character. The PR_{NTO} values, obtained at MR-CISD level of theory, are shown in Fig. 4 for all structures. Numerical PR_{NTO} values obtained at MR-CISD, ADC(2) and TDDFT levels of theory are collected for all structures in Tables S2–S14 (ESI†) and the stacked PR_{NTO} value plots for ADC(2) and TD-DFT levels of theory are shown in Fig. S1 (ESI†). As mentioned above, these data indicate how many major configurations are necessary to characterize each of the studied excited states. One can see that for the pristine periacene, each of the excited states require at least two essential configurations. BN-center, BN-edges and BN-edges-line structures show only one main configuration for the S_1 state. As BN-vertical S_1 and BN-center S_3 cases are fully characterized by a double excitation, as shown in Fig. 5, a PR_{NTO} value cannot be defined for these states, given that the contribution of the one-particle transition density matrix vanished in these cases. With the exception of the states dominated by double excitations, the ADC(2) and TD-DFT PR_{NTO} values show good agreement with the reference pattern obtained at the MR-CISD level, although they slightly underestimate it.

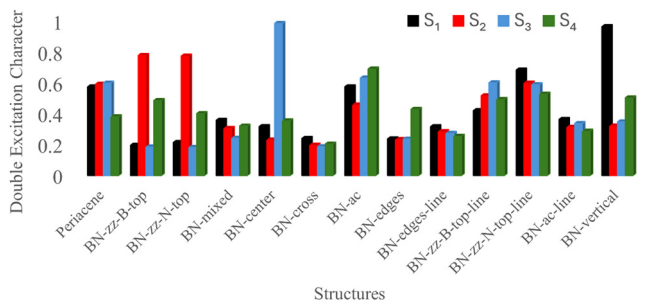

Fig. 5 Double excitation character for all computed excited states and all structures, obtained at MR-CISD level of theory.

Inspection of the double excitation character displayed in Fig. 5 shows that most of the excited states possess substantial double excitation character (numerical values are given in Table S15, ESI†). The outstanding examples are the S_3 state of the BN-center structures and the S_1 state of the BN-vertical case with around 100% double excitation character, but also the S_2 states of the BN-zz-B-top and BN-zz-N-top structures have dominating double excitation character (above 70%). On the other hand, for the BN-zz-B-top, BN-zz-N-top, BN-mixed, BN-center, BN-cross, BN-edges, BN-edges-line and BN-ac-line structures, at least one excited state is found with a lower proportion of double-excitation character, using a 30% threshold. A comprehensive analysis reveals that, out of the 52 excited states characterized, only 17 falls below the 30% threshold. It is then confirmed that, in general, for nearly all the proposed structures, the examined excited states exhibit a significant double-excitation character.

For the periacene, BN-ac, BN-vertical, and BN-edges-line structures, we were unable to perform ADC(2) calculations because the D1 diagnostic values, for the preceding MP2 calculation, were significantly higher than the recommended threshold value of 0.04.[72] The need for a multireference approach for these high D1 cases was confirmed by the relatively small weight of the ground state dominant electronic configurations, using MR-CISD, of 32%, 60%, 28.0% and 57%, respectively as detailed in Tables S16–S19 (ESI†), together with their respective D1 values. Across nearly all analyzed structures, the D1 values approached the established limit of 0.04 for reliable accuracy of single-reference methods. This highlights the necessity of multireference theory to accurately characterize these types of structures.

3.2 Charge transfer and natural transition orbitals

According to Kasha's rule,[73] the high-lying excited states should quickly decay *via* internal conversion to the S_1 state, highlighting that the main phases of a given photocatalytic reaction are expected to occur in the first excited state. Therefore, structures possessing a CT state at S_1 are of special interest for photocatalytic processes. NTOs were used to visualize the electronic transitions and to quantify their character according to local excitation (LE) or CT. To perform this analysis the localization of the hole and electron were determined in the doped periacene sheets using always a division into three segments as shown, *e.g.*, in Fig. 7. The segmentation was performed by assigning the uppermost row labeled as segment 1, the middle one as segment 2, and the bottom row as segment 3. The three segments define a 3×3 Ω matrix according to eqn (1) with the diagonal elements corresponding to local excitations and the off-diagonal ones to CT.

Fig. 6 shows the NTOs obtained at MR-CISD level for the BN-center structure. The S_1 state is represented by an excitation with the hole in the bottom row (segment 3, see segment numbering in Fig. 7) and the electron in the uppermost row (segment 1), representing a CT (segments 3-1) state. The first number in this notation indicates the hole segment and the second number the electron segment of the NTO. The S_2 and S_4

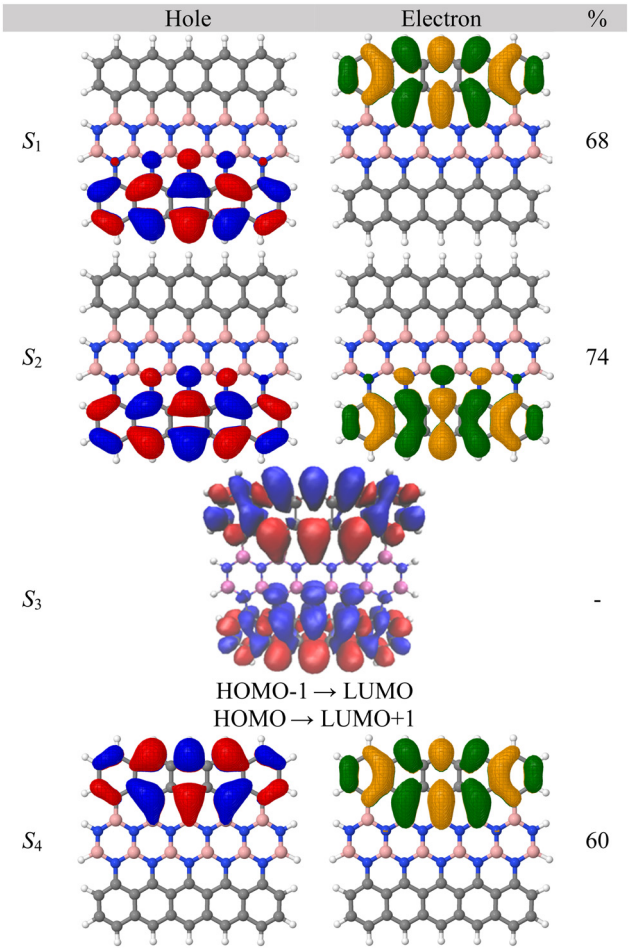

Fig. 6 BN-center NTOs obtained at the MR-CISD level of theory, for the transition to the S_1, S_2 and S_4 states. (isovalue ±0.04 e bohr^{-3}). S_3 state consists of a double excitation (HOMO−1 → LUMO, HOMO → LUMO+1), the density difference between this state and S_0 was plotted in this case (isovalue of ±0.0005 e bohr^{-3}) and the red color means a decrease in electron density, while blue indicates that the density increased.

states are characterized as local excitations, on segments 3 and 1, respectively, whilst S_3 is dominated by a double excitation (HOMO−1 to LUMO in fragment 1 and HOMO to LUMO+1 in fragment 3), NTOs cannot be calculated for this excited state because the one-particle density matrix vanishes in this case. Instead, the charge density difference of the related orbitals is plotted in Fig. 7 for this state, showing a superposition of two locally excited regions.

The NTOs obtained at ADC(2) level (Fig. S2, ESI†) for the BN-center structure present a CT state (segments 3-1) in S_1 and a LE state for S_2 (segment 3-3), in agreement with MR-CISD results. The ADC(2) method exhibits another CT state (segments 1-3) for the S_4 state. TD-DFT results show a different state ordering by exhibiting a LE state (segment 3-3) for S_1 and the CT state (segments 3-1) in S_2 state (see Fig. S3, ESI†). The S_4 state is a LE state at TD-DFT level, as also shown by the MR-CISD results. The S_3 state is a doubly excited state and cannot be well characterized by either by ADC(2) nor TD-DFT levels of theory, that only shows one half (LE segment 1-1) of the total double excitation.

The quantitative data shown in the state composition bar plot for the BN-center doped structure calculated at the MR-CISD level (Fig. 7) shows good agreement with the qualitative analysis of the NTOs given in the previous paragraph. The S_1 state is dominated by a CT transition from segment 3 to segment 1. Local excitations in segment 3 and 1 dominate S_2 and S_4, respectively. The double excitation character of the S_3 state is clearly indicated as well. Results computed at ADC(2) level (Fig. S4a, ESI†) correctly show CT character for S_1 and LE character for S_2 states. It shows half of the double excitation (LE segment 1-1) for the S_3 and indicates a CT state for the S_4 state, which is not in agreement with the MR-CISD results. Regarding the TD-DFT (Fig. S4b, ESI†), a reordering of the state character with respect to the MR-CISD results is found. The character of the S_1 and S_2 states is reversed. S_1 is a LE state and S_2 a CT state. Also, only half of the double excitation character is seen for the S_3 state (LE segment 1-1) and S_4 is a LE state (segment 3-3).

The NTOs for the BN-vertical doped structure, at MR-CISD level, are shown in Fig. 8 and the segmentation definition is displayed in Fig. 9. The S_1 state of the BN-vertical structure has a strong double excitation character (HOMO^2 → LUMO^2) and, therefore, its NTOs cannot be accessed, instead the charge

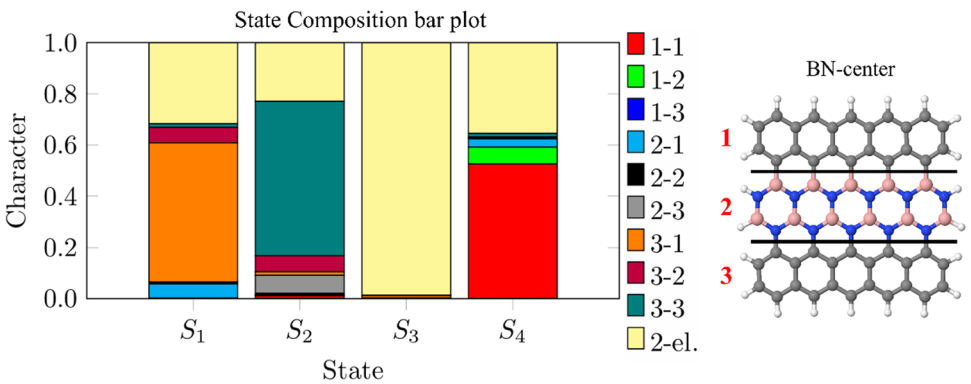

Fig. 7 The first four singlet excited states, obtained at MR-CISD level, for the BN-center structure decomposed into contributions of local excitations (LE), charge transfer (between segments) and double excitations (2-el.). The segments division is indicated by numbers in red.

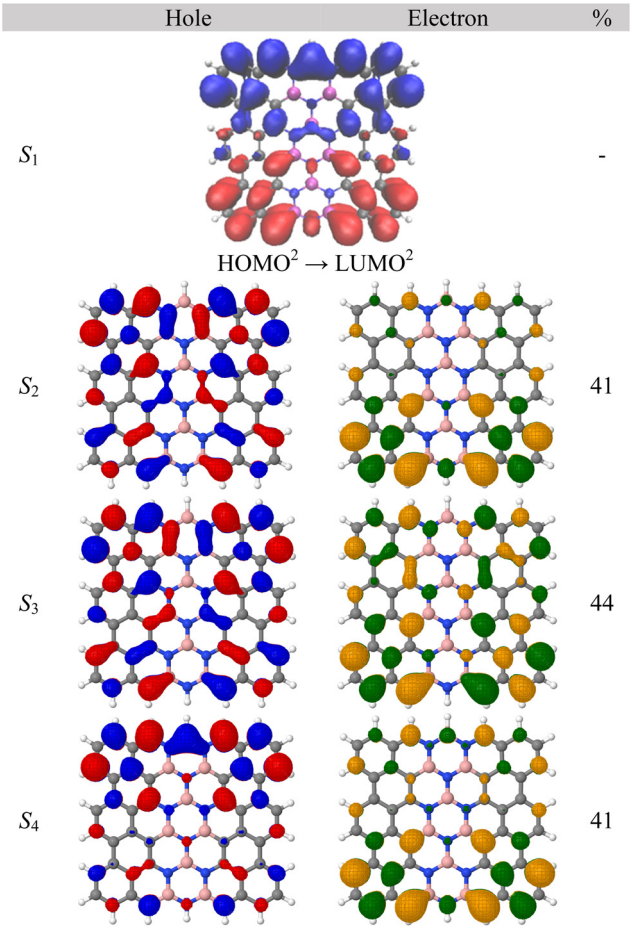

Fig. 8 BN-vertical NTOs obtained at the MR-CISD level of theory, for the transition to the S_2, S_3 and S_4 states. (isovalue ±0.04 e bohr^{-3}). S_1 state consists of a double excitation ($HOMO^2 \rightarrow LUMO^2$), the density difference between this state and S_0 was plotted in this case (isovalue of ±0.0005 e bohr^{-3}) and the red color means a decrease in electron density, while blue indicates that the density increased.

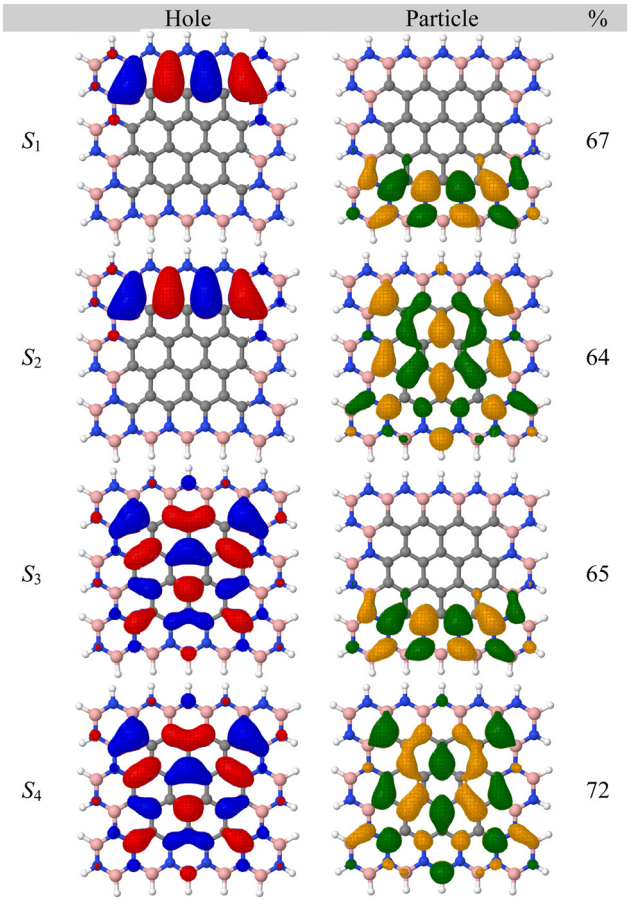

Fig. 10 BN-edges-line NTOs obtained at the MR-CISD level of theory, for the transition to all four studied singlet excited states (isovalue ±0.04 e bohr^{-3}).

density difference is plot in Fig. 8. In contrast to the doubly excited state characterized for the BN-center S_3 state (Fig. 6), the case here demonstrates that doubly excited states can have also CT character (segment 3 to 1). It is noted at this point that double excitations might not be uncommon in doped PAHs as they had been observed in several instances of N-doped pyrene as well.[21] The S_2, S_3 and S_4 states are characterized as a mixture of different contributions, without a predominant one. As previously explained, ADC(2) calculations were not performed for BN-vertical due to the elevated D1 diagnostic value. The NTOs obtained at TD-DFT level are shown in Fig. S5 (ESI†)

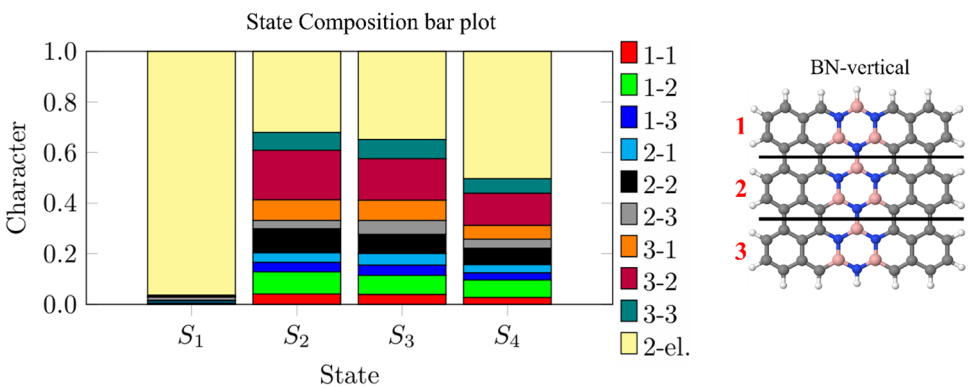

Fig. 9 The first four singlet excited states, obtained at MR-CISD level, for the BN-vertical structure decomposed into contributions of local excitations (LE), charge transfer (between segments) and double excitations (2-el.). The segments division is indicated by numbers in red.

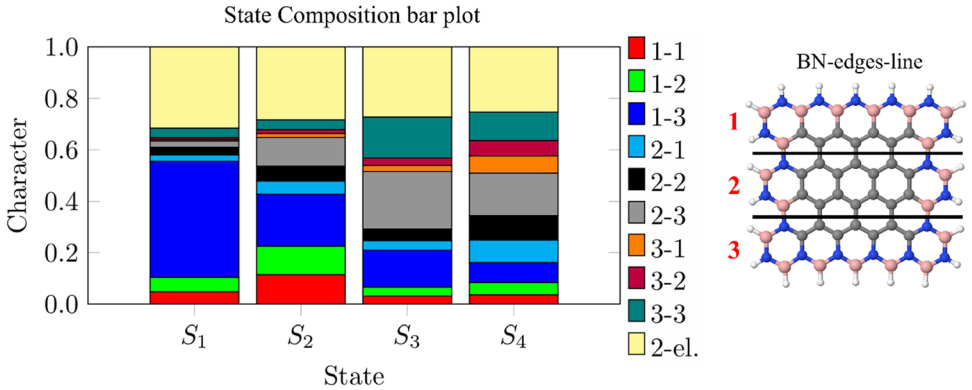

Fig. 11 The first four singlet excited states, obtained at MR-CISD level, for the BN-edges-line structure decomposed into contributions of local excitations (LE), charge transfer (between segments) and double excitations (2-el.). The segments division is indicated by numbers in red.

and all the four computed singlet excited states exhibit a combination of different contributions, without a strongly predominant one, in accordance with the results obtained from the MR-CISD for S_2, S_3, and S_4. The S_1 state exhibits only half of the total contribution from segment 3 to 1 (singly excited).

The state composition diagram for the BN-vertical structure, obtained at MR-CISD level (Fig. 9), shows also that the S_1 state has a dominating double excitation character, while the other states have strongly mixed contributions as already found with the above discussion of the NTOs, with no prevailing one. The state composition diagram obtained at TD-DFT level (Fig. S6, ESI†) shows no prevailing contribution for all four excited states analyzed, agreeing with what was previously shown by the TD-DFT NTOs.

From the proposed B/N line-pairs modified structures, only BN-edges-line presents a CT state for S_1. Fig. 10 collects the MR-CISD NTOs for this case. The segment numbering can be found in Fig. 11. The S_1 state exhibits segment 1 to segment 3 CT state. The other states, S_2, S_3 and S_4, are delocalized. Given that BN-edges-line was also one of the structures with an elevated D1 diagnostic value, as BN-vertical, ADC(2) method could not be performed. The NTOs obtained at TD-DFT level are shown in Fig. S7 (ESI†). Their analysis, as happened to the BN-center case, shows different ordering for the CT state characterization. The CT state (segments 1-3) is the S_2, while the mixture of composition contributions (mainly segments 1-2 and 1-3) is the S_1 state, while S_3 and S_4 states follow the delocalized pattern observed in the MR-CISD results.

In agreement with the MR-CISD NTOs, the bar composition plot for the BN-edges-line (Fig. 11), obtained at MR-CISD level, shows that the S_1 state is related to the transfer from segment 1 to segment 3. A collection of different contributions, without a dominating one, characterizes the other excited states. TD-DFT analytical results (Fig. S8, ESI†) indicate a reordering between S_1 and S_2, when compared to MR-CISD, and shows no predominant contribution for the other states.

Achieving a well-separated electron–hole pair is essential for the potential generation of oxidation–reduction agents in photocatalytic processes. Notably, all three structures exhibiting a charge-transfer (CT) state in the S_1 state demonstrated this separation. Although, it is important to mention that the BN-vertical bright state is a little below the VR light range (Fig. 3), but this structure probably has other bright states, beyond S_4, which are within the VR range and can be populated to decay to S_1. Also, one can note that independently of the type of inserted topology, the structures that have a S_1 CT state show an excitation from one extreme segment to the other edge of the structure.

Regarding the other doped structures presented in this work, for which charge transfer states were not identified as the first excited state, the state composition bar plot obtained at MR-CISD level, can be found in Fig. S9 (ESI†). They show a mixture of a variety of state characters, with only S_3 for BN-cross having a pronounced CT character.

4. Conclusions

The first four low-lying singlet excited states of a (5a,5z) periacene and a series of 12 different B/N doped periacene structures were investigated at MR-CISD, SC-NEVPT2, ADC(2) and TD-DFT levels of theory with the goal of characterizing these states accurately in terms of LE and CT states. The doping was achieved either by bisecting the periacene with borazine chains or by B/N lines. Most interest was dedicated to CT states in S_1 since from there, according to Kasha's rule, long-time photodynamic would start. Analysis of the MR-CISD electronic wavefunctions for the ground state and of transition density matrices between ground and excited states for periacene and the doped structures showed that several of the ground states possessed MR character and that the excited states had substantial double excitation character. SC-NEVPT2 calculations confirmed these observations. These findings make the application of popular SR and TD-DFT methods problematic. Selected LE and CT states could in principle be reproduced by ADC(2) and TD-DFT calculations even though they were hampered by the missing substantial double excitation character included in these states. States dominated by double excitations could not be reproduced at all by these two methods.

It was found that the BN-center, BN-vertical and BN-edges-line doped structures possessed a CT state for S_1. This fact makes them potential candidates for photocatalytic processes. The last two structures show excitation energies around and below 0.5 eV. This energetic proximity to the ground state makes them good candidates for ultrafast radiationless deactivation to S_0, a process which would obstruct the planned photocatalytic reactions in S_1. The BN-center structure, however, seems to be a good candidate possessing CT character and sufficient stability in S_1 to act as initiator for electron donor and electron acceptor processes. The computed S–T splittings support the mentioned trends: BN-center shows a large S–T splitting (1.34 eV). In contrast, BN-vertical (0.33 eV) and BN-edges-line (0.07 eV) exhibit small S–T splittings. These observations reinforce BN-center as the most promising structure for sustaining photocatalytic activity in the S_1 state. For the BN-center S_3 state and BN-vertical S_1 state the dominating double-excitation character of the wavefunctions lead to vanishing the one-particle transition density and density difference analysis was performed to establish the character of the state. It is interesting to note that in the latter structural case (BN-vertical) the S_1 CT state was a doubly excited state which might lead to different properties toward interaction with reaction partners that usual single excitations do. This is a point to be to be investigated in further research. The CT states showed strong separation at the far-end edges of the doped periacene sheets. This is an important feature for electron transfer interactions for both reduction and oxidation reactions in the context of photocatalysis, for example.

Author contributions

Luan G. F. dos Santos: performance of calculation, data collection and analysis; Julio C. V. Chagas and Reed Nieman: support in data analysis; Adelia J. A. Aquino: contribution to manuscript writing and editing; Francisco B. C. Machado: contribution to project conceptualization; Hans Lischka: Supervision and final manuscript preparation.

Data availability

See the ESI† for Cartesian coordinates of all structures, comparison of excited states energies, oscillator strength (f) and PR_{NTO} values obtained at the different levels of theory. The numerical values of the doubly excitation character, the ground state dominant electron configurations (for special cases) are also shown. For the S_1 CT (BN-center, BN-vertical and BN-edges-line) structures, the comparison between the methods in terms of NTOs and bar composition plots of the excited states are also exhibited.

Conflicts of interest

There are no conflicts to declare.

Acknowledgements

Financial assistance of Brazilian agencies Conselho Nacional de Desenvolvimento Científico e Tecnológico (CNPq) under project no. 307168/2022-0, 164766/2021-9, Fundação de Amparo à Pesquisa do Estado de São Paulo (FAPESP) under project no. 2022/16385-8, and Coordenação de Aperfeiçoamento de Pessoal de Nível Superior (CAPES) under project no. 88887.877979/2023-00 and 88881.799245/2022-01 are gratefully acknowledged. We are thankful for the supply of computer time at the HPCC facilities of Texas Tech University. L. G. F. dS. expresses gratitude for the Helen DeVitt Jones Graduate Fellowship offered by the Texas Tech University Graduate School.

References

1 F. Chien, H. W. Kamran, G. Albashar and W. Iqbal, *Int. J. Hydrogen Energy*, 2021, **46**, 7745–7758.
2 H. Song, S. Luo, H. Huang, B. Deng and J. Ye, *ACS Energy Lett.*, 2022, **7**, 1043–1065.
3 S. Chu and A. Majumdar, *Nature*, 2012, **488**, 294–303.
4 N. Lu, M. Zhang, X. Jing, P. Zhang, Y. Zhu and Z. Zhang, *Energy Environ. Mater.*, 2023, **6**, e12338.
5 J. Low, J. Yu, M. Jaroniec, S. Wageh and A. A. Al-Ghamdi, *Adv. Mater.*, 2017, **29**, 1601694.
6 D. A. Panayotov, A. I. Frenkel and J. R. Morris, *ACS Energy Lett.*, 2017, **2**, 1223–1231.
7 R. Ameta, M. S. Solanki, S. Benjamin and S. C. Ameta, *Adv. Oxid. Processes Water Wastewater Treat.*, 2018, **1**, 135–175.
8 C. Byrne, G. Subramanian and S. C. Pillai, *J. Environ. Chem. Eng.*, 2018, **6**, 3531–3555.
9 I. I. Alkhatib, C. Garlisi, M. Pagliaro, K. Al-Ali and G. Palmisano, *Catal. Today*, 2020, **340**, 209–224.
10 Y. Zhang, H. Liu, F. Gao, X. Tan, Y. Cai, B. Hu, Q. Huang, M. Fang and X. Wang, *EnergyChem*, 2022, **4**, 100078.
11 K. Li, B. Peng and T. Peng, *ACS Catal.*, 2016, **6**, 7485–7527.
12 X. Chen, J. Zhao, G. Li, D. Zhang and H. Li, *Energy Mater.*, 2022, **2**, 200001.
13 C. Aumaitre and J. F. Morin, *Chem. Rec.*, 2019, **19**, 1142–1154.
14 J. Wagner, P. Zimmermann Crocomo, M. A. Kochman, A. Kubas, P. Data and M. Lindner, *Angew. Chem., Int. Ed.*, 2022, 134.
15 L. Zhang, Y. Cao, N. S. Colella, Y. Liang, J.-L. Brédas, K. N. Houk and A. L. Briseno, *Acc. Chem. Res.*, 2015, **48**, 500–509.
16 J. Kumar, B. Basu, F. A. Talukdar and A. Nandi, *J. Electromagn. Waves Appl.*, 2017, **31**, 2046–2054.
17 B. Milián-Medina and J. Gierschner, *Org. Electron.*, 2012, **13**, 985–991.
18 T. Mahmoudi, Y. Wang and Y.-B. Hahn, *Nano Energy*, 2018, **47**, 51–65.
19 R. Rieger and K. Müllen, *J. Phys. Org. Chem.*, 2010, **23**, 315–325.
20 X. Feng, V. Marcon, W. Pisula, M. R. Hansen, J. Kirkpatrick, F. Grozema, D. Andrienko, K. Kremer and K. Müllen, *Nat. Mater.*, 2009, **8**, 421–426.

21 X. Shao, A. J. A. Aquino, M. Otyepka, D. Nachtigallová and H. Lischka, *Phys. Chem. Chem. Phys.*, 2020, **22**, 22003–22015.
22 J. M. Farrell, C. Mützel, D. Bialas, M. Rudolf, K. Menekse, A.-M. Krause, M. Stolte and F. Würthner, *J. Am. Chem. Soc.*, 2019, **141**, 9096–9104.
23 T. Huang, Z. Ding, H. Liu, P.-A. Chen, L. Zhao, Y. Hu, Y. Yao, K. Yang and Z. Zeng, *Chin. Chem. Lett.*, 2024, **35**, 109117.
24 M. Pinheiro, L. F. A. Ferrão, F. Bettanin, A. J. A. Aquino, F. B. C. Machado and H. Lischka, *Phys. Chem. Chem. Phys.*, 2017, **19**, 19225–19233.
25 T. Agou, J. Kobayashi and T. Kawashima, *Chem. Commun.*, 2007, 3204–3206.
26 P.-A. Bouit, A. Escande, R. Szűcs, D. Szieberth, C. Lescop, L. Nyulászi, M. Hissler and R. Réau, *J. Am. Chem. Soc.*, 2012, **134**, 6524–6527.
27 S. M. Draper, D. J. Gregg and R. Madathil, *J. Am. Chem. Soc.*, 2002, **124**, 3486–3487.
28 A. A. Gorodetsky, C. Y. Chiu, T. Schiros, M. Palma, M. Cox, Z. Jia, W. Sattler, I. Kymissis, M. Steigerwald and C. Nuckolls, *Angew. Chem., Int. Ed.*, 2010, **49**, 7909–7912.
29 W. Jiang, H. Qian, Y. Li and Z. Wang, *J. Org. Chem.*, 2008, **73**, 7369–7372.
30 J. Wei, B. Han, Q. Guo, X. Shi, W. Wang and N. Wei, *Angew. Chem., Int. Ed.*, 2010, **49**, 8209–8213.
31 D. Wu, W. Pisula, M. C. Haberecht, X. Feng and K. Müllen, *Org. Lett.*, 2009, **11**, 5686–5689.
32 R. J. Kahan, W. Hirunpinyopas, J. Cid, M. J. Ingleson and R. A. W. Dryfe, *Chem. Mater.*, 2019, **31**, 1891–1898.
33 M. Laghaei, M. Ghasemian, W. Lei, L. Kong and Q. Chao, *J. Mater. Chem. A*, 2023, **11**, 11925–11963.
34 M. Li, Y. Wang, P. Tang, N. Xie, Y. Zhao, X. Liu, G. Hu, J. Xie, Y. Zhao, J. Tang, T. Zhang and D. Ma, *Chem. Mater.*, 2017, **29**, 2769–2776.
35 M. Lu, J. Liu, Q. Li, M. Zhang, M. Liu, J. L. Wang, D. Q. Yuan and Y. Q. Lan, *Angew. Chem., Int. Ed.*, 2019, **58**, 12392–12397.
36 S. Barman, A. Singh, F. A. Rahimi and T. K. Maji, *J. Am. Chem. Soc.*, 2021, **143**, 16284–16292.
37 J. Qiu, Y. Zheng, L. Wang, M. Liu, L. Tian, X. Yu, X. An and G. Lv, *J. Mater. Chem. A*, 2023, **11**, 4572–4578.
38 Y. Zheng, Y. Jiao, L. Ge, M. Jaroniec and S. Z. Qiao, *Angew. Chem., Int. Ed.*, 2013, **52**, 3110–3116.
39 B. D. Milanez, G. M. dos Santos, M. Pinheiro, L. T. Ueno, L. F. A. Ferrão, A. J. A. Aquino, H. Lischka and F. B. C. Machado, *J. Comput. Chem.*, 2023, **44**, 755–765.
40 J.-L. Brédas, J. E. Norton, J. Cornil and V. Coropceanu, *Acc. Chem. Res.*, 2009, **42**, 1691–1699.
41 M. Bendikov, H. M. Duong, K. Starkey, K. N. Houk, E. A. Carter and F. Wudl, *J. Am. Chem. Soc.*, 2004, **126**, 7416–7417.
42 F. Plasser, H. Pašalić, M. H. Gerzabek, F. Libisch, R. Reiter, J. Burgdörfer, T. Müller, R. Shepard and H. Lischka, *Angew. Chem., Int. Ed.*, 2013, **52**, 2581–2584.
43 J. Hachmann, J. J. Dorando, M. Avilés and G. K. Chan, *J. Chem. Phys.*, 2007, **127**, 134309.
44 A. Sánchez-Grande, J. I. Urgel, L. Veis, S. Edalatmanesh, J. Santos, K. Lauwaet, P. Mutombo, J. M. Gallego, J. Brabec, P. Beran, D. Nachtigallová, R. Miranda, N. Martín, P. Jelínek and D. Écija, *J. Phys. Chem. Lett.*, 2021, **12**, 330–336.
45 S. Das and J. Wu, *Phys. Sci. Rev.*, 2017, **2**, 20160109.
46 B. Shi, D. Nachtigallová, A. J. A. Aquino, F. B. C. Machado and H. Lischka, *J. Chem. Phys.*, 2019, **150**, 124302.
47 J.-D. Chai and M. Head-Gordon, *Phys. Chem. Chem. Phys.*, 2008, **10**, 6615.
48 F. Weigend and R. Ahlrichs, *Phys. Chem. Chem. Phys.*, 2005, **7**, 3297–3305.
49 P. G. Szalay, T. Müller, G. Gidofalvi, H. Lischka and R. Shepard, *Chem. Rev.*, 2012, **112**, 108–181.
50 H. Lischka, D. Nachtigallová, A. J. A. Aquino, P. G. Szalay, F. Plasser, F. B. C. Machado and M. Barbatti, *Chem. Rev.*, 2018, **118**, 7293–7361.
51 J. A. Pople, R. Seeger and R. Krishnan, *Int. J. Quantum Chem*, 1977, **12**, 149–163.
52 J. Schirmer, *Phys. Rev. A: At., Mol., Opt. Phys.*, 1982, **26**, 2395–2416.
53 A. B. Trofimov and J. Schirmer, *J. Phys. B: At. Mol. Opt. Phys.*, 1995, **28**, 2299–2324.
54 C. Angeli, R. Cimiraglia, S. Evangelisti, T. Leininger and J. P. Malrieu, *J. Chem. Phys.*, 2001, **114**, 10252–10264.
55 C. Hättig and F. Weigend, *J. Chem. Phys.*, 2000, **113**, 5154–5161.
56 A. Köhn and C. Hättig, *J. Chem. Phys.*, 2003, **119**, 5021–5036.
57 A. Das, T. Müller, F. Plasser and H. Lischka, *J. Phys. Chem. A*, 2016, **120**, 1625–1636.
58 R. Ditchfield, W. J. Hehre and J. A. Pople, *J. Chem. Phys.*, 1971, **54**, 724–728.
59 F. Plasser and H. Lischka, *J. Chem. Theory Comput.*, 2012, **8**, 2777–2789.
60 F. Plasser, S. A. Bäppler, M. Wormit and A. Dreuw, *J. Chem. Phys.*, 2014, **141**, 024107.
61 S. Tretiak and S. Mukamel, *Chem. Rev.*, 2002, **102**, 3171–3212.
62 M. T. do Casal, J. M. Toldo, M. Barbatti and F. Plasser, *Chem. Sci.*, 2023, **14**, 4012–4026.
63 R. L. Martin, *J. Chem. Phys.*, 2003, **118**, 4775–4777.
64 H. Lischka, T. Müller, P. G. Szalay, I. Shavitt, R. M. Pitzer and R. Shepard, *Wiley Interdiscip. Rev.: Comput. Mol. Sci.*, 2011, **1**, 191–199.
65 H. Lischka, R. Shepard, T. Müller, P. G. Szalay, R. M. Pitzer, A. J. A. Aquino, M. M. Araújo do Nascimento, M. Barbatti, L. T. Belcher, J.-P. Blaudeau, I. Borges, Jr., S. R. Brozell, E. A. Carter, A. Das, G. Gidofalvi, L. González, W. L. Hase, G. Kedziora, M. Kertesz, F. Kossoski, F. B. C. Machado, S. Matsika, S. A. do Monte, D. Nachtigallová, R. Nieman, M. Oppel, C. A. Parish, F. Plasser, R. F. K. Spada, E. A. Stahlberg, E. Ventura, D. R. Yarkony and Z. Zhang, *J. Chem. Phys.*, 2020, **152**, 134110.
66 F. Neese, *Wiley Interdiscip. Rev.: Comput. Mol. Sci.*, 2022, **12**, e1606.
67 S. G. Balasubramani, G. P. Chen, S. Coriani, M. Diedenhofen, M. S. Frank, Y. J. Franzke, F. Furche, R. Grotjahn, M. E. Harding, C. Hättig, A. Hellweg, B. Helmich-Paris, C. Holzer, U. Huniar, M. Kaupp, A. Marefat Khah, S. Karbalaei Khani, T. Müller, F. Mack, B. D. Nguyen,

S. M. Parker, E. Perlt, D. Rappoport, K. Reiter, S. Roy, M. Rückert, G. Schmitz, M. Sierka, E. Tapavicza, D. P. Tew, C. van Wüllen, V. K. Voora, F. Weigend, A. Wodyński and J. M. Yu, *J. Chem. Phys.*, 2020, **152**, 184107.
68 F. Plasser, *J. Chem. Phys.*, 2020, **152**, 084108.
69 L. G. F. dos Santos, J. C. V. Chagas, L. F. A. Ferrão, A. J. A. Aquino, R. Nieman, H. Lischka and F. B. C. Machado, *J. Comput. Chem.*, 2025, **46**, e70039.
70 S. C. Bhatia, in *Advanced Renewable Energy Systems*, ed. S. C. Bhatia, Woodhead Publishing, India, 2014, vol. 2, pp. 32–67.
71 U. Hochkirch, W. Herrmann, R. Stosser, H.-H. Borchert and M. Linscheid, *Spectrosc. Int. J.*, 2006, **20**, 1–17.
72 A. E. Torres, P. Guadarrama and S. Fomine, *J. Mol. Model.*, 2014, **20**, 2208.
73 M. Kasha, *Discuss. Faraday Soc.*, 1950, **9**, 14–19.